Corrosion Protection Characteristics of Doped Magnetite Layers on Carbon Steel Surfaces in Aqueous CO2 Environments

Joshua Owen, Francois Ropital, Gaurav R. Joshi, Jean Kittel, Richard Barker

Journal of Pipeline Science and Engineering 4 (2024) 100199

Contents lists available at ScienceDirect

Journal of Pipeline Science and Engineering

journal homepage: www.keaipublishing.com/en/journals/journal-of-pipeline-science-and-engineering/

Corrosion protection characteristics of doped magnetite layers on carbon steel surfaces in aqueous CO_2 environments

Joshua Owen [a,*], Francois Ropital [b,c], Gaurav R. Joshi [b], Jean Kittel [b], Richard Barker [a]

[a] Institute of Functional Surfaces, School of Mechanical Engineering, University of Leeds, Leeds, LS2 9JT, United Kingdom
[b] IFP Energies Nouvelles, Rond-point de l'échangeur de Solaize, BP 3, 69360 Solaize, France
[c] Univ. Lyon, INSA-Lyon, MATEIS UMR CNRS, Bât Blaise Pascal, 7 Avenue Jean Capelle, F-69621 Villeurbanne Cedex, France

ARTICLE INFO

Keywords:
Carbon steel
Magnetite
Electrochemical impedance spectroscopy
Electrodeposition
Localised corrosion
CO_2 corrosion

ABSTRACT

Magnetite (Fe_3O_4) corrosion product surface layers can limit uniform corrosion rates of carbon steel in aqueous carbon dioxide (CO_2)-saturated environments. However, as Fe_3O_4 is a semiconductor, localised corrosion can proceed due to galvanic interaction between the Fe_3O_4 layers and bare steel. In this study, metal dopants were integrated into Fe_3O_4 layers to mitigate the effects of localised corrosion, whilst maintaining its protective barrier properties. Model Fe_3O_4 and metal-doped Fe_3O_4 layers were electrodeposited on carbon steel and immersed in a pH 5, 1 wt% sodium chloride (NaCl), CO_2-saturated, 50 °C solution. Under the conditions studied, the incorporation of magnesium into the Fe_3O_4 layer resulted in reduced localised corrosion when the 3D surface profiles of the underlying carbon steel were measured using white light interferometry.

1. Introduction

Magnetite (Fe_3O_4) is an inverse spinel crystalline iron oxide with electrical semiconductor and magnetic properties (Verwey and Heilmann, 1947). Fe_3O_4 layers can form naturally on steel surface under certain conditions, and are widely found on iron-based materials in a number of applications, including on carbon steel in carbon dioxide (CO_2) saturated environments (Hua et al., 2019; Thorhallsson et al., 2020; de Motte et al., 2020; Barker et al., 2018; Mundhenk et al., 2020; Tanupabrungsun et al., 2013), stainless steel and carbon steel in nuclear applications (Jaffré et al., 2021; Song et al., 2018) and on carbon steel in anoxic environments (Mercier-Bion et al., 2018). Fe_3O_4 behaves as both an N or P-type semiconductor, having a reported resistivity of the order of 10^{-2} to 10^{-1} Ω cm and a band gap of 0.1 eV (Itai et al., 1971; Xu and Schoonen, 2000). The intrinsic semi-conductive properties of the Fe_3O_4 layers on steel surfaces are important in the study of corrosion, as Fe_3O_4 can readily establish a galvanic couple with the less noble steel substrate. This leads to aggressive enhanced corrosion rates of the bare (i.e., uncovered by Fe_3O_4) carbon steel in instances where there is partial coverage of the layer (Hua et al., 2019; Song et al., 2018; Gonzalez et al., 2021; Owen et al., 2022a). Despite the consequences associated with localised corrosion in the presence of Fe_3O_4 layers in CO_2-saturated environments (Hua et al., 2019; Owen et al., 2023), there is still a lack of consensus around the role that Fe_3O_4 plays on both uniform and localised corrosion of carbon steel under these conditions. Furthermore, to our knowledge there have been no known attempts to modify the structure of the Fe_3O_4 layer with corrosion protection in mind. This study addresses such possibilities, motivated by the success associated with iron carbonate ($FeCO_3$) corrosion product layer modification that has resulted in enhanced corrosion protection of carbon steel (Shaikhah et al., 2022).

Structural modification of corrosion layers on carbon steel surfaces can result in significantly different physical properties and corrosion protection characteristics. This process can be engineered, whereby a dopant is added to the local environment and integrated within the layer (Shaikhah et al., 2022), or occur naturally, due to the presence of metal ions in solution (Hua et al., 2018) and/or metal alloying elements (Ko et al., 2015). CO_2 corrosion environments, such as those found in geothermal energy extraction, typically contain a wide range of metal cations that can integrate within corrosion product layers, such as magnesium (Hua et al., 2018), calcium (Matamoros-Veloza et al., 2020; Shamsa et al., 2019; Jacklin et al., 2022), manganese (Mundhenk et al., 2013), copper and zinc (Sanjuan et al., 2016), to name a few. The composition of Fe_3O_4 can be influenced by these metal ions (Suresh et al., 2016), which can have a significant influence on layer conductivity (He et al., 2013), and crystal structure and morphology (Owen et al., 2023), which in turn has an important influence on galvanic corrosion with carbon steel (Owen et al., 2022a, 2023). The possible benefits to corrosion protection of modified Fe_3O_4 layers on carbon steel

* Corresponding author.
E-mail address: J.J.Owen@leeds.ac.uk (J. Owen).

https://doi.org/10.1016/j.jpse.2024.100199
Received 19 January 2024; Received in revised form 11 June 2024; Accepted 14 June 2024
Available online 16 June 2024

surfaces are yet to be studied in detail but are common in other applications, such as nanoparticle development for catalysts (Orooji et al., 2020) and medical coating applications (O'Hara et al., 2016; de Mello et al., 2019).

Of particular interest in this study is the role of modified Fe_3O_4 surface layers on carbon steel in CO_2 corrosion environments. CO_2 corrosion occurs because of $CO_{2(g)}$ dissolving in water to form carbonic acid, which partially dissociates to produce hydrogen ions (H^+) and carbonate species. When galvanic corrosion proceeds in the presence of electrical conductivity between Fe_3O_4 and bare carbon steel, H^+ is reduced at the Fe_3O_4 surface in the cathodic reaction:

$$2\ H^+_{(aq)} + 2\ e^- \rightarrow H_{2(g)} \quad (1)$$

Consequently, the anodic dissolution of the bare steel surface is enhanced, producing iron cations (Fe^{2+}) via the anodic equation, summarised by:

$$Fe_{(s)} \rightarrow Fe^{2+}_{(aq)} + 2\ e^- \quad (2)$$

The general mechanism of Fe_3O_4 formation in a CO_2 system (i.e., conditions favourable to the production Fe^{2+} cations via Eq. (2)) is attributed to the following reaction:

$$3\ Fe^{2+}_{(aq)} + 4\ H_2O_{(aq)} \rightarrow Fe_3O_{4(s)} + 8\ H^+_{(aq)} + 2\ e^- \quad (3)$$

In aqueous CO_2 conditions, Fe_3O_4 is commonly found at temperatures >120 °C, near-neutral pH and lower partial pressures of CO_2, becoming more thermodynamically stable as temperature increases (Tanupabrungsun et al., 2012). The formation of Fe_3O_4 on carbon steel surfaces in CO_2 environments is also occasionally observed concomitantly with $FeCO_3$ growth at temperatures <120 °C (de Motte et al., 2020; Basilico et al., 2021; Han et al., 2009). The reasons for the lack of understanding of Fe_3O_4 behaviour are, therefore, potentially explained by the high temperatures necessary to produce Fe_3O_4 layers in CO_2 environments and the simultaneous growth/revealing of other surface layers, such as iron carbide (Fe_3C) (Owen et al., 2022a; Crolet et al., 1998; Farelas et al., 2010) and $FeCO_3$ (Hua et al., 2019; de Motte et al., 2020; Tanupabrungsun et al., 2013), making it difficult to attribute corrosion mechanisms to Fe_3O_4 alone. An alternative method to produce Fe_3O_4 layers on carbon steel surfaces in short periods at ambient pressure in controlled environments is via electrodeposition (Song et al., 2018; Owen et al., 2022a). The application of a cathodic potential for 30 min to an electrode immersed in a 2 M sodium hydroxide (NaOH), triethanolamine (TEA), ferric sulphate ($Fe_2(SO_4)_3$) solution produces crystalline Fe_3O_4 on the electrode surface with varying characteristics, depending on the solution temperature (60–90 °C) (Kothari et al., 2006). This technique has been used to electrodeposit Fe_3O_4 on carbon steel (Song et al., 2018; Owen et al., 2022a; Jeon et al., 2015), stainless steel (Kulp et al., 2009), nickel alloys (Goujon et al., 2015) and gold (Kulp et al., 2009; Bhat et al., 2017) substrates. Another major advantage of this technique is that the electrolyte composition can be varied to produce mixed metal Fe_3O_4 layers (Beal et al., 2017).

The general mechanism proposed for the electrodeposition of Fe_3O_4 is that the Fe^{3+} ions are complexed by TEA and subsequently reduced to Fe^{2+} at the substrate surface upon the application of a potential (Kulp et al., 2009; Lê et al., 2019). Complexed Fe^{3+} remains in solution near to the substrate surface, resulting in the formation of Fe_3O_4, incorporating both Fe^{2+} and Fe^{3+} in the crystal structure, via Reaction (5) (Bhat et al., 2017):

$$Fe(III) - TEA + e^- \leftrightharpoons Fe(II) - TEA \quad (4)$$

$$Fe(II) - TEA + 2\ Fe(III) - TEA + 8\ OH^- \leftrightharpoons Fe_3O_4 + 3\ TEA + 4\ H_2O \quad (5)$$

In this study, Fe_3O_4 layers and Fe_3O_4 modified through the incorporation of metal ions into the crystal structure and formed by electrodeposition were evaluated for corrosion protection of carbon steel in CO_2-saturated environments. The addition of manganese, magnesium and zinc metal ions into the Fe_3O_4 was investigated. These metals were chosen based on previous doped magnetite electrodeposition studies and successful complexation of their metal ions in TEA (Beal et al., 2017; Ishikawa et al., 1999; Sen and Dotson, 1970; Karadag et al., 2001; Switzer et al., 2010). However, literature reporting on mixed Fe_3O_4 layers formed on carbon steel surfaces is scarce, and there are no reported studies on the influence of such layers on corrosion behaviour. The electrodeposited layers on carbon steel were characterised using surface analytical techniques before immersion in an aqueous CO_2-saturated environment to assess the extent of corrosion protection provided by the modified layers. In-situ electrochemical measurements and post-experimental surface analysis were performed to characterise the general and localised corrosion behaviour of the underlying carbon steel.

2. Experimental procedure

2.1. Material preparation

The X65 carbon steel used in this study had a ferrite-pearlite microstructure and composition (wt%) of Fe (97.8), C (0.15), Mn (1.42), Ni (0.09), Nb (0.054), Mo (0.17), Si (0.22), V (0.06), P (0.025) and S (0.02). Coupons were machined into 6 mm thick discs (dia.=12 mm). To facilitate electrochemical measurements by using the carbon steel coupons as working electrodes, an insulated copper wire was soldered to the reverse side of the coupon before embedding in a non-conductive epoxy resin (resulting an exposed surface area of 1.13 cm^2). Coupons were prepared for experiments by wet grinding using P180, P320 and P600 grit silicon carbide (SiC) paper progressively, before rinsing with acetone and deionised water, prior to drying with compressed air.

2.2. Electrodeposition

For electrodeposition of Fe_3O_4, coupons were immersed in a 2 M NaOH, 1 M TEA, 0.043 M hydrated $Fe_2(SO_4)_3$ solution, heated to 80 °C in a glass beaker placed on a hot plate. The solution was gently stirred using a magnetic stirrer. A cathodic potential of −1.05 V vs. silver/silver chloride (Ag/AgCl) reference electrode was applied to the X65 steel coupon (used as the working electrode), utilising a combination Ag/AgCl reference and platinum (Pt) counter electrode to complete the three-electrode cell. Within an applied potential range from −1.00 $V_{Ag/AgCl}$ to −1.05 $V_{Ag/AgCl}$, the structure and composition of electrodeposited Fe_3O_4 layers has been shown not to vary significantly when deposited on stainless steel (Kulp et al., 2009) and nickel-based alloys (Goujon et al., 2015). On stainless steels within this potential range, Kulp et al. (2009) showed using Mossbauer spectroscopy that the proportion of Fe^{3+} in tetrahedral sites of the Fe_3O_4 crystal structure accounted for 26%–29% of the overall crystal composition, with the remainder split between Fe^{2+} and Fe^{3+} in octahedral sites. At more cathodic potentials, the proportion of Fe^{3+}in octahedral sites was significantly reduced (below −1.05 $V_{Ag/AgCl}$, attributed to enhanced reduction of Fe^{3+} at the substrate surface and sulphate green rust is produced (below −1.10 $V_{Ag/AgCl}$) or pure iron deposited (below −1.20 $V_{Ag/AgCl}$) (Kulp et al., 2009). To create mixed Fe_3O_4 layers, the alternative metal sulphates were mixed in solution with the $Fe_2(SO_4)_3$ at a ratio of 25 mol% of metal sulphate to 75 mol% $Fe_2(SO_4)_3$ in a one-step electrochemical-chemical deposition process (He et al., 2013). Hydrated magnesium sulphate ($MgSO_4$), zinc sulphate ($ZnSO_4$) and manganese sulphate ($MnSO_4$) were used in this study.

To optimise the deposition protocol when metal dopants were added to the solution, cyclic voltammetry (CV) measurements were performed in the same experimental conditions. A gold electrode (surface area 0.02 cm^2) was employed as the working electrode as part of a three-electrode cell and stirring was stopped prior to starting measurements. A scan rate of 50 mV/s in a potential range from −0.4 $V_{Ag/AgCl}$ to −1.2 $V_{Ag/AgCl}$ was utilised. Results are shown in the Supplementary Material. As the NaOH-TEA solution is electrochemically inactive (Kulp et al., 2009), any reduction and

oxidation events were attributed to reactions occurring at the surface involving the complexed metal ions to form Fe_3O_4 or doped Fe_3O_4. CV results confirmed that the same cathodic potential of $-1.05\ V_{Ag/AgCl}$ could be applied to the X65 steel coupon to electrodeposit the doped Fe_3O_4 layers.

2.3. CO_2 corrosion experiments

After the layers had been electrodeposited, coupons were removed from the electrodeposition solution, dried using a heat gun (to minimise solution contamination during further experiments) and transferred into a glass beaker, shown in Fig. 1, containing a 600 mL deionised water, 1 wt % sodium chloride (NaCl) solution, saturated with CO_2-saturated and adjusted to pH 5 with a fixed quantity of sodium hydrogen carbonate. The solution was prepared by bubbling CO_2 into a sealed container for a minimum period of 12 h prior to transfer of the solution into the experimental beaker shown in Fig. 1 under the pressure of the CO_2 gas. The test coupons were immersed in the solution once the temperature reached 50 °C, controlled by flow from an oil bath around the jacketed glass cell. The solution pH was confirmed once the solution was heated to 50 °C using an automatic temperature compensation pH probe. Layered coupons were compared against the behaviour of a bare X65 carbon steel coupon under the same conditions over 4 h and 24 h of immersion.

In the pH 5, 50 °C conditions, the dissolution of Fe_3O_4 was anticipated due to the temperature and pH being lower than those typical for Fe_3O_4 formation in CO_2-saturated environments (Sweeton et al., 1970). However, localised corrosion is most likely to occur when only partial coverage is achieved on the surface. Partial coverage would be expected in conditions where the layer is growing or where the layer has been removed from the surface through chemical dissolution, with the latter scenario created at pH 5 and a temperature of 50 °C in a CO_2-saturated solution. Furthermore, these conditions avoid the growth of $FeCO_3$ layers on the surface in atmospheric pressure CO_2-saturated conditions, due to the high concentrations of Fe^{2+} required to achieve supersaturation and hence precipitation of $FeCO_3$ (Barker et al., 2018). This was particularly relevant during experiment design to avoid ambiguity during the interpretation of data. Furthermore, this solution chemistry also enabled a direct comparison to be made with other studies by the authors (Owen et al., 2022a). As growth of Fe_3O_4 is not expected in these conditions, the durability of the layers could be thoroughly evaluated.

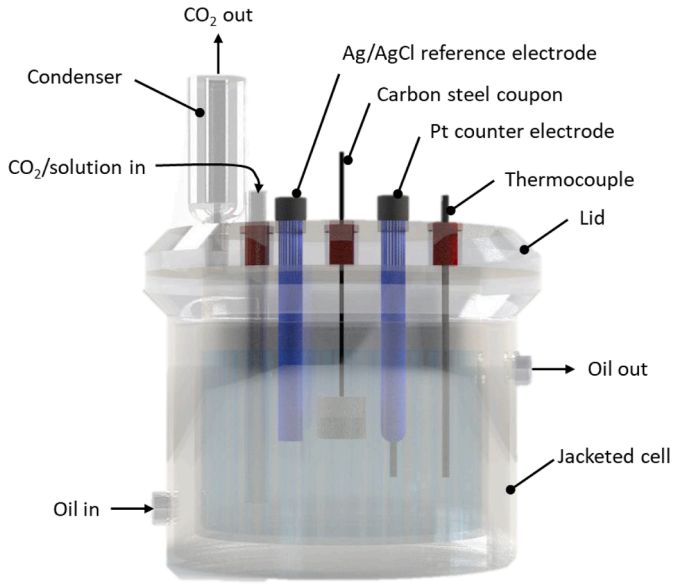

Fig. 1. Experimental setup for CO_2 corrosion assessment of bare carbon steel and Fe_3O_4 layers.

Experiments were also performed using bare carbon steel to enable a direct comparison to be made with the layered coupons.

2.4. Electrochemical techniques

To complete the three-electrode cell, an Ag/AgCl reference electrode and Pt wire counter electrode were used and connected to a potentiostat (Biologic). The X65 steel working electrode (with and without electrodeposits) was placed adjacent to the reference and counter electrodes to minimise ohmic drop during electrochemical measurements. Linear polarisation resistance (LPR) measurements were performed every 2 h (starting after 15 min of immersion) by scanning from −15 mV to +15 mV vs. open circuit potential (OCP) at a scan rate of 0.25 mV/s. Electrochemical impedance spectroscopy (EIS) measurements were performed after LPR measurements (and a 5 min period to allow OCP to stabilise) by applying a sinusoidal potential between ±10 mV vs. OCP over a frequency range from 20,000 Hz to 0.01 Hz, with 10 measurements per frequency decade. The raw data was initially analysed by performing a Kramers-Kronig transformation in EC-Lab software, utilising the methodology of Boukamp (1995), to identify erroneous data points to be removed from further analysis. Equivalent electrical circuits were then constructed and the values of the components of the circuits were determined using Measurement Model software (Watson and Orazem, 2020).

Potentiodynamic polarisation measurements at the end of 4 h and 24 h experiments (undertaken in separate experiments with different durations) enabled a comparison of the anodic and cathodic behaviour of the layered coupons, by scanning from +5 mV to −250 mV vs. OCP during the cathodic scan, followed by scanning from −5 mV to +250 mV vs. OCP at a scan rate of 0.5 mV/s. OCP was monitored in between all measurements, including a 5 min period between the cathodic and anodic potentiodynamic polarisation scans. Surface analysis was not performed on coupons that were subject to potentiodynamic polarisation measurements.

2.5. Surface analysis

Surface analysis of electrodeposited coupons was performed to characterise the nature of the formed layers before and after CO_2 corrosion experiments. Coupons, utilised for EIS and LPR measurements only, were removed from the electrodeposition solution, immediately dried, broken out of the epoxy resin and stored under vacuum until analyses were performed. XRD patterns were obtained on a 10 mm×10 mm region in the centre of the coupon using a Bruker D8 diffractometer, scanning across a 2 θ range of 20° to 70° at a step size of 0.032 °/s. International Centre for Diffraction Data (ICDD) references were used to identify Fe_3O_4 (00-001-1111), $MnFe_2O_4$ (01-071-4919), $MgFe_2O_4$ (00-036-0398) and $ZnFe_2O_4$ (00-001-1109) peaks.

An FEI Helios G4 CX DualBeam FIB-SEM was utilised to obtain top-view and cross-section SEM images of the coupons in secondary electron mode at an operating voltage of 5.0 kV and working distance of 4 mm. Coupons were carbon coated before mounting in the instrument. To cross section the coupons, a Pt layer was deposited first on the top surface using a gallium ion beam at an operating current of 0.23 nA, before a series of cross-sectioning (operating current 21 nA) and surface cleaning (operating current 2.5 nA) were performed using the ion beam, orientated at 52° to the coupon. These processes enabled a 15 µm wide, 10 µm deep cross section to be imaged using SEM. Images of the cross-sections were obtained using the gallium ion beam at an operating current of 7.7 pA.

Localised corrosion information was obtained by profiling the surface of the carbon steel surfaces under the layer. Firstly, layers were removed by sonicating coupons in a hydrochloric acid solution containing the corrosion inhibitor hexamethylenetetramine, according to ASTM International standard G1-03 (2017). The coupons were removed from the solution, cleaned with deionised water, and dried prior to analysis. Three 1×1 mm^2 regions of the carbon steel surface were

scanned using a Bruker NPFLEX white light interferometer to obtain a 3D profile of the surface. Raw data were filtered using the Vision64 software and pit-like features were identified on the surface by implementing threshold depth criteria. Based on the method implemented by Shamsa et al. (2019), the top ten deepest pit-like features were selected, with an average of those values taken to determine a penetration depth.

3. Results and discussion

3.1. Characterisation of electrodeposited layers

To establish Fe_3O_4 and doped Fe_3O_4 layers on carbon steel surfaces, X65 carbon steel coupons were immersed in the gently stirred electrodeposition solution. Upon immersing the coupon, a constant potential of -1.05 $V_{Ag/AgCl}$ was applied for a period of 30 min to electrodeposit the Fe_3O_4 and mixed Fe_3O_4 layers. The chronoamperogram for each electrodeposited layer is shown in Fig. 2, reported as an average of at least three measurements with error bars representing the standard deviation. Relatively constant current densities were observed throughout the 30 min period.

Once the layers had been deposited, coupons were removed from solution and prepared either for ex-situ analysis to characterise the nature of the electrodeposited layers or for immersion experiments. XRD patterns were obtained to confirm the crystalline structure of the layers, with diffractograms presented in Fig. 3. At a 2 θ position of $\approx 45°$, the peak for α-Fe was observed on all coupons, representing the carbon steel substrate. The most dominant peaks on the electrodeposited Fe_3O_4 diffractogram were the (311) at 2 $\theta \approx 35°$ and (400) at 2 $\theta \approx 43°$ crystal planes. Diffraction patterns were similar between all the materials analysed. Due to the similarity in ICDD references between Fe_3O_4 and mixed metal Fe_3O_4, notable differences were not anticipated. However, the addition of metal dopants into the crystal structure resulted in broadening, shifting and/or additional peaks observed in Fig. 3(b) and (c). Small peak shifts were also observed in another study where metal dopants (Zn, Mn) were integrated into the Fe_3O_4 structure (de Mello et al., 2019).

SEM and FIB analysis of the electrodeposited layers were performed to characterise the surface coverage, layer thickness and nature of the crystal structure in Fig. 4. A wide coverage of closely packed crystals was observed in the layers across the surface area in all electrodeposited coupons, with no obvious regions of exposed steel. For undoped Fe_3O_4, a mixture of larger crystals ($\approx$ 4 μm in average lateral size) and smaller crystals closer to the surface (<1 μm in average lateral size) was observed consistently across the surface. The physical characteristics of the Fe_3O_4 layer were very similar to those formed naturally in 48 h on X65 carbon steel under aqueous CO_2 conditions representative of geothermal environments (pH 7.5, 45 bar, 0.3 wt% NaCl, 250 °C) (Owen et al., 2023). The thickness of the Fe_3O_4 layer, as determined by FIB imaging, was approximately 2.1±0.6 μm. For each coupon investigated, the microstructure of the underlying carbon steel could be observed because of etching from the ion beam. Near to the surface at the interface with the Fe_3O_4 layers, a thin region of finer crystals is observed due to work hardening of the surface during wet grinding prior to electrodeposition.

The addition of metal ions into the crystal structure of the Fe_3O_4 had

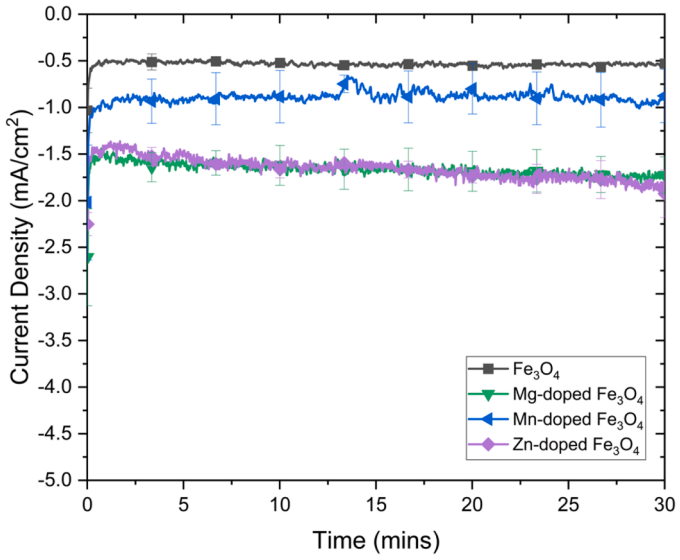

Fig. 2. Chronoamperogram of Fe_3O_4 and doped Fe_3O_4 electrodeposition on X65 carbon steel at a potential of −1.05 mV vs. Ag/AgCl over a period of 30 min in 2 M NaOH, 1 M TEA solutions at 80 °C containing metal sulphates.

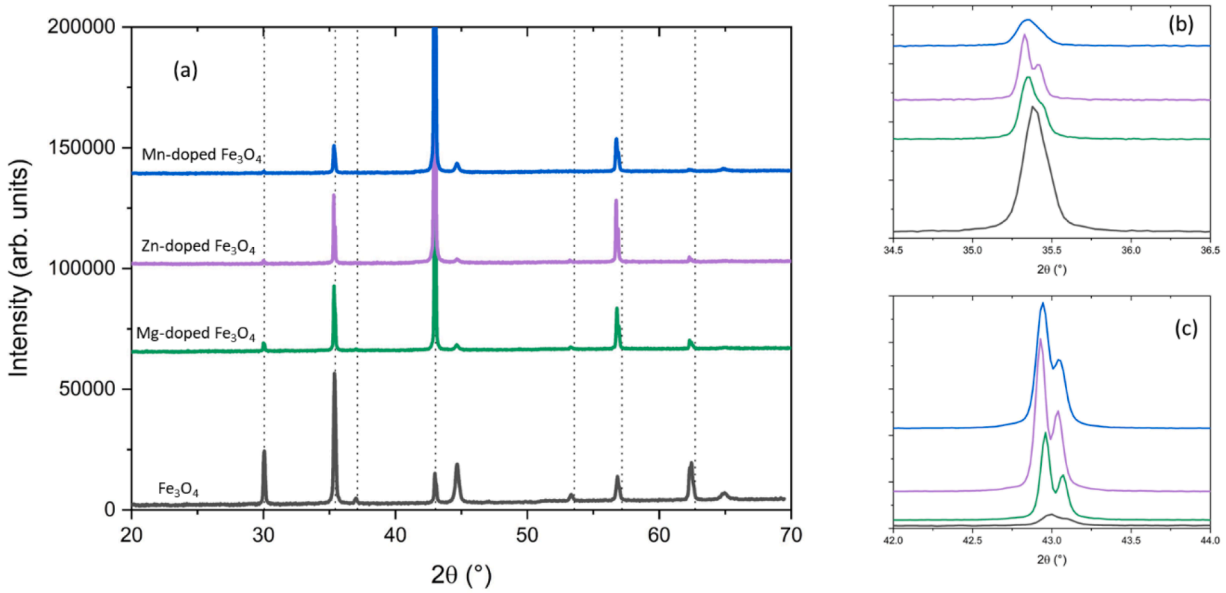

Fig. 3. XRD patterns collected from Fe_3O_4 and doped Fe_3O_4 layers electrodeposited on X65 carbon steel surfaces in 2 M NaOH, 1 M TEA solutions at 80 °C containing metal sulphates showing (a) the full scan range, (b) detailed analysis of the (311) peak and (c) detailed analysis of the (400) peak.

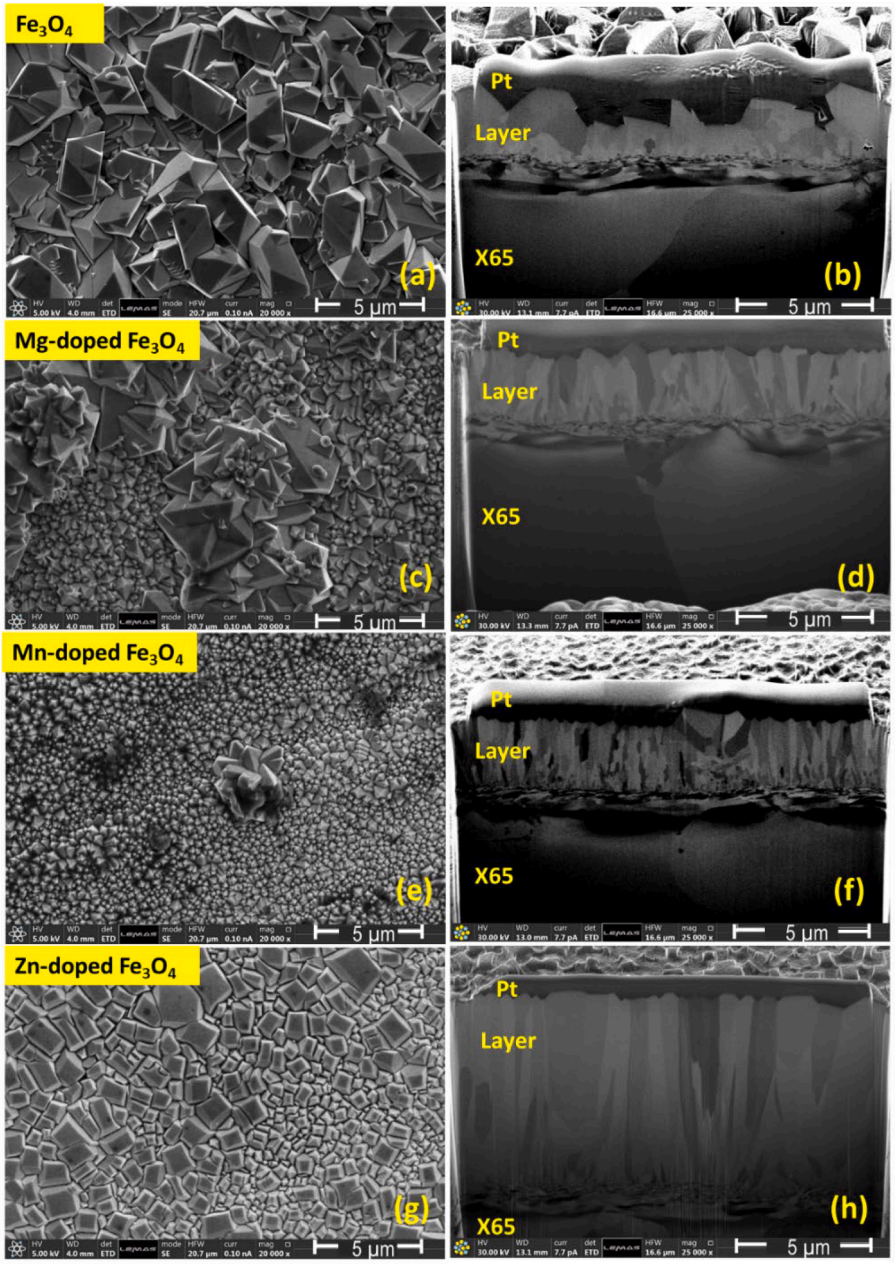

Fig. 4. (a, c, e, g) SEM top view and (b, d, f, h) gallium beam images obtained after FIB cross-sectioning of the electrodeposited layers on carbon steel surfaces, showing (a, b) Fe_3O_4-layered X65, (c, d) Mg-doped Fe_3O_4-layered X65, (e, f) Mn-doped Fe_3O_4-layered X65 and (g, h) Zn-doped Fe_3O_4-layered X65 coupons.

a significant effect on the characteristics of the layers. Similar changes in Fe_3O_4 crystal morphology have been reported upon the addition of small quantities of other metal ions (Co, Cu, Cr) (Ishikawa et al., 1999). Generally, the doped magnetite layers showed elongated, columnar structures. The Mg-doped Fe_3O_4 layer was composed of similar crystals to the Fe_3O_4 layer, but with fewer larger crystals (about 1.3 µm in average lateral size) and a greater proportion of smaller crystals (<1 µm in average lateral size). The thickness of the Mg-doped Fe_3O_4 layer, was approximately 2.7±0.2 µm, similar to the thickness of the Mn-doped Fe_3O_4 layer, which had a thickness of 2.8±0.3 µm. The effect of Mn doping produced mainly small-sized crystals (about 0.75 µm in average lateral size), with few larger crystals. Zn doping had the most significant effect on the layer characteristics, causing a considerable change in the habit of the crystals and the form of the overlayer, with an average lateral size of 2.1 µm. The produced layer was also considerably thicker than the other layers, with a thickness of 7.5±0.3 µm determined from FIB imaging.

3.2. CO_2 corrosion evaluation

Corrosion experiments were subsequently performed on bare X65 carbon steel and with the electrodeposited layers to evaluate the corrosion resistance provided to the X65 carbon steel substrate. The electrodeposited layers were prepared immediately before each experiment and were not reused in any experiment. The behaviour over a 24 h period in the pH 5, CO_2-saturated solutions measured by LPR is shown in Fig. 5. Results are reported as the reciprocal of charge transfer resistance (R_{ct}), to avoid introducing inaccuracies through the determination of a Stern-Geary coefficient that would likely vary during the experiments. In this initial approach, the parameter of $1/R_{ct}$ is directly proportional to

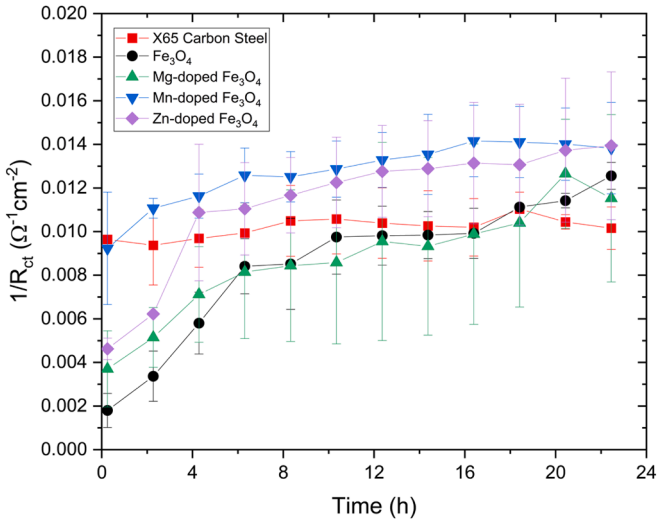

Fig. 5. Reciprocal of charge transfer resistance (directly proportional to corrosion rate) determined from LPR measurements performed in a 50 °C, pH 5, 1 wt% NaCl solution on bare X65 carbon steel and X65 carbon steel covered with electrodeposited Fe_3O_4, Mg-doped Fe_3O_4, Mn-doped Fe_3O_4 and Zn-doped Fe_3O_4 layers.

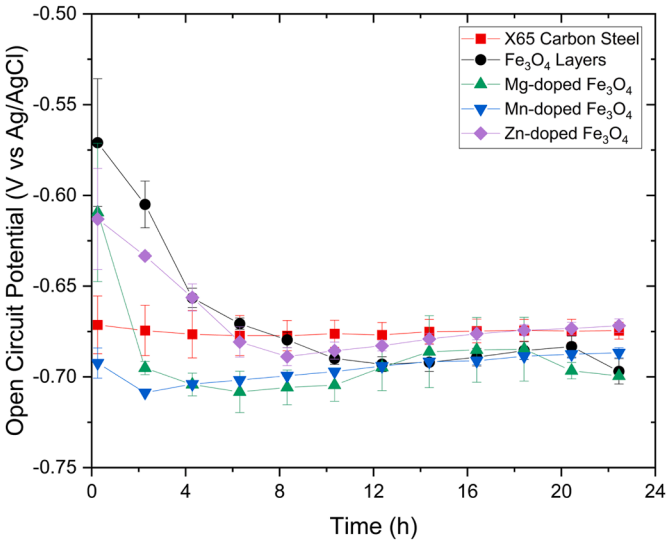

Fig. 6. OCP measurements in a 50 °C, pH 5, 1 wt% NaCl solution on bare X65 carbon steel and X65 carbon steel covered with electrodeposited Fe_3O_4, Mg-doped Fe_3O_4, Mn-doped Fe_3O_4 and Zn-doped Fe_3O_4 layers.

corrosion rate. The value of $1/R_{ct}$ was determined by subtracting the electrolyte resistance (R_e), obtained from EIS measurements (reported later), from polarisation resistance (R_p) measurements. An average of $1/R_{ct}$ is reported from a minimum of two repeat measurements, with error bars representing the maximum and minimum values. The bare X65 carbon steel showed a marginal increase in $1/R_{ct}$ throughout the experiment, attributed to the progressive revealing of the Fe_3C network from the carbon steel microstructure as a result of preferential dissolution of the ferrite phase (Farelas et al., 2010; Owen et al., 2022b).

When comparing measurements during the first 4 h of the experiment, carbon steel layered with Fe_3O_4, Mg-doped Fe_3O_4 and Zn-doped Fe_3O_4 experienced a reduced corrosion rate, attributed to the protection provided by the layers. The Fe_3O_4 and Mg-doped Fe_3O_4 showed similar behaviour, reducing $1/R_{ct}$ by approximately 60–80% compared to bare steel, before $1/R_{ct}$ gradually increased. These values were equivalent to bare carbon steel after approximately 12 h. The layers, therefore, showed limited durability due to conditions being more favourable for the dissolution of Fe_3O_4 as opposed to its growth. However, the harsh conditions for Fe_3O_4 stability enabled the relative resilience of each layer to be assessed. Zn-doped Fe_3O_4 also provided some corrosion protection, in a similar manner to Fe_3O_4 and Mg-doped Fe_3O_4, but the durability of the Zn-doped Fe_3O_4 layers was much reduced, with $1/R_{ct}$ exceeding those for bare steel after approximately 4 h. The greater thickness of the Zn-doped layer did not appear to have a noticeable influence on corrosion protection. Mn-doped Fe_3O_4 layers provided no corrosion protection to the carbon steel, with higher values of $1/R_{ct}$ compared to bare steel observed throughout the 24 h experiment.

OCP was also monitored throughout the experiment and is shown for each material electrodeposit in Fig. 6. The OCP of the bare carbon steel was stable at approximately -0.675 $V_{Ag/AgCl}$ throughout the 24 h experiment. A minor increase in OCP was observed, consistent with the revealing of the Fe_3C network (Owen et al., 2022b). The OCP for layered coupons (except for Mn-doped Fe_3O_4) was more positive than bare X65 carbon steel initially, anticipated due to the wide lateral coverage of Fe_3O_4 and doped Fe_3O_4 layers and the more noble OCP of Fe_3O_4 compared to bare steel (Owen et al., 2022b; Alam et al., 2016). The OCP decreased for the layered coupons in a similar manner to the change in behaviour of $1/R_{ct}$ observed in Fig. 5, converging to the bare carbon steel. It would suggest that these layers progressively dissolved. A previous study assessing the galvanic coupling between these layers and bare carbon steel has indicated that the mixed potential of the layers is in the range of -0.65 $V_{Ag/AgCl}$ to -0.70 $V_{Ag/AgCl}$ (Owen et al., 2022a), suggesting the behaviour observed in Fig. 6 could be attributed to either partial coverage or no coverage of the various Fe_3O_4 layers, once a steady OCP was measured in this range.

Potentiodynamic polarisation measurements were performed at the end of 24 h experiments, in addition to experiments completed over a 4 h duration. The potentiodynamic polarisation data were corrected to account for solution resistance and are shown in Fig. 7. Approximations of corrosion current density (i_{corr}), OCP and the anodic (β_a) and cathodic (β_c) Tafel constants are reported in Table 1 after interpretation of the potentiodynamic polarisation plots. OCP data and the general trend of corrosion current densities correlated with the results reported in Figs. 5 and 6. The OCP values did not change significantly between those measurements at 4 h and 24 h, except for Zn-doped Fe_3O_4. However, only a slight change in OCP was observed for Zn-doped Fe_3O_4 (-0.036 $V_{Ag/AgCl}$), similar to the change demonstrated in Fig. 6. Anodic and cathodic Tafel constants were obtained at approximately ± 50 mV vs. OCP. The Tafel constants did not change significantly over the duration of the test, with only subtle differences observed between measurements after 4 h and 24 h. No significant differences were identified between the layered coupons and bare steel. The corrosion current densities after 4 h were lower for pure Fe_3O_4 (0.071 mA/cm^2) and Zn-doped Fe_3O_4 (0.097 mA/cm^2) than bare carbon steel (0.136 mA/cm^2), confirming a reduction in corrosion rate in the presence of the layers. By the end of the 24 h experiments, corrosion current densities for layered coupons were higher than bare carbon steel, suggesting an appreciable increase in corrosion rate as dissolution of the layer progressed. Minor differences were observed between the different layers, however, this may be due to variation that is typical in the identification of Tafel constants and a corrosion current density from potentiodynamic polarisation data.

3.3. EIS analysis

LPR measurements demonstrated the comparable behaviour of the bare steel and layered coupons over the duration of the experiment but do not provide a mechanistic understanding of the layers' behaviour. EIS enables a more thorough understanding of the behaviour of surface

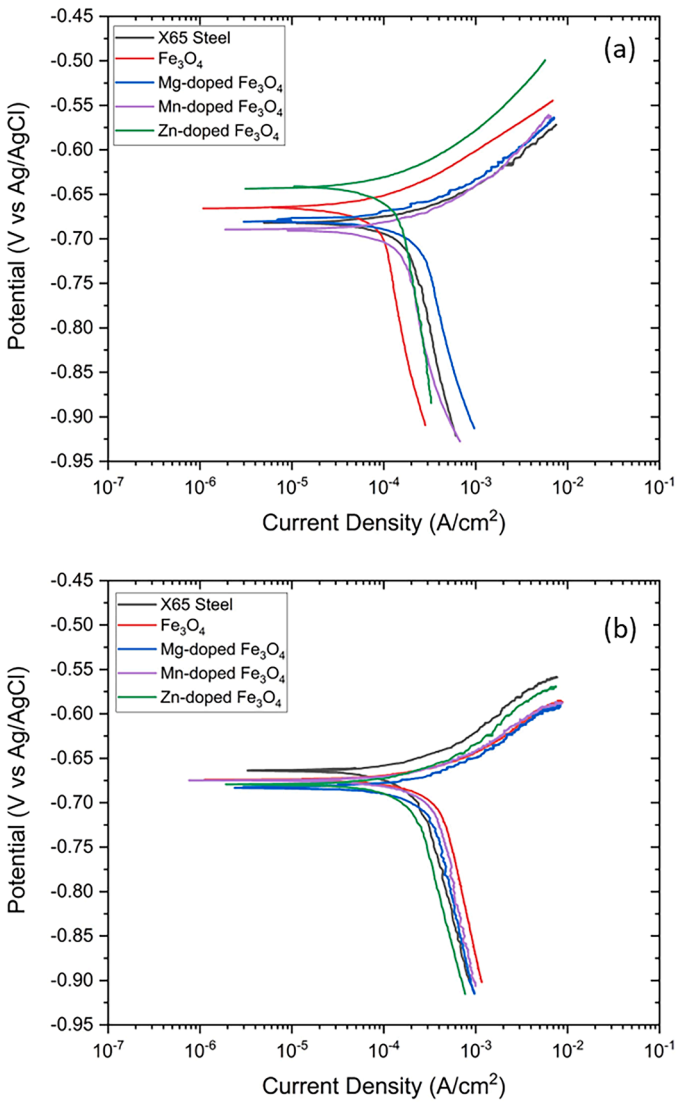

Fig. 7. Potentiodynamic polarisation plots measured after (a) 4 h and (b) 24 h of exposure to a 50 °C, pH 5, 1 wt% NaCl solution for bare X65 carbon steel, Fe_3O_4-layered X65, Mg-doped Fe_3O_4-layered X65, Mn-doped Fe_3O_4-layered X65 and Zn-doped Fe_3O_4-layered X65 coupons.

layers on carbon steel behaviour to be established (de Motte et al., 2020; Farelas et al., 2010; Lazareva et al., 2021) and has been used to characterise Fe_3O_4 layers on carbon steel surfaces previously (Das and Sudersanan, 2003; Park and Macdonald, 1983). Data from EIS measurements are shown in the form of a Nyquist plot in Fig. 8 and a Bode phase angle plot in Fig. 9, reporting data over 24 h of immersion in the pH 5, CO_2-saturated, 1 wt% NaCl solution at 50 °C. Plots are shown at 0 h (i.e., approximately 20 min after immersion), 2 h, 4 h and 22 h, with the focus being the initial part of the experiment (before significant dissolution of the layers) and the behaviour towards the end of the experiment. Bode magnitude plots are presented in the Supplementary Material. The phase angle was adjusted (φ_{adj}) to account for the electrolyte resistance (R_e) using Eq. (6).

$$\varphi_{adj} = \tan^{-1}\frac{Z''}{Z' - R_e} \quad (6)$$

Where Z' and Z'' are the real and imaginary components of impedance (Ω cm^2), respectively.

Focusing on bare X65 carbon steel, this material showed the typical behaviour of an actively corroding material in the absence of a protective surface layer (de Motte et al., 2020; Farelas et al., 2010). A single time constant loop is observed, expected to represent the charge transfer processes involved in the corrosion reactions and the capacitance of the electrical double layer. Initially R_{ct} is around 110 Ω cm^2, which is comparable to R_{ct} determined from LPR measurements (about 105 Ω cm^2). The diameter of the Nyquist plot decreased during the experiment to about 80–100 Ω cm^2, consistent with LPR measurements, indicating a decrease in charge transfer resistance, and so an increase in corrosion rate.

Similar shaped Nyquist data were also observed for layered coupons with no additional features. At early exposure times, the layered surfaces present depressed semicircles that are either similar in magnitude to the initial X65 steel impedance (i.e., the Mn-doped and Zn-doped Fe_3O_4) or 2–3 times greater (Fe_3O_4 and Mg-doped Fe_3O_4). Consistent and similar trends in R_{ct} were observed when comparing EIS and LPR measurements. However, some discrepancy was observed in initial measurements that are likely explained by the longer duration of EIS measurements. Over the 24 h exposure, the impedances of all electrodes decreased to 80–100 Ω cm^2 range, indicative of the Fe_3O_4 dissolution process.

It is possible that the capacitance could be a mixture of: 1) the double layer capacitance at the steel surface, 2) the double layer capacitance at the Fe_3O_4 surface, and 3) capacitance of the layer itself. Other studies of Fe_3O_4 layers on carbon steel have indicated the presence of a second capacitance loop, typically in the high frequency domain, attributed to capacitive behaviour of the Fe_3O_4 layer (Alam et al., 2016; Park and Macdonald, 1983). Additional capacitance loops have also been observed in the high frequency portion of EIS data speculated to be caused by trace amounts of thin (10–100 nm) Fe_3O_4 deposits on carbon steel surfaces in aqueous CO_2 environments (de Motte et al., 2020). These features were not observed on the layered coupons in Fig. 8, possibly due to the thickness of the layers observed from cross-sectional imaging. Additionally, the theoretical capacitance of an equivalent porous surface film, C_{layer}, is shown to negligible (about 10 nF/cm^2) using Eq. (7) (Orazem and Tribollet, 2008):

Table 1
Analysis of data obtained from potentiodynamic polarisation measured after 4 h and 24 h of exposure to a 50 °C, pH 5, 1 wt% NaCl solution for bare X65 carbon steel, Fe_3O_4-layered X65, Mg-doped Fe_3O_4-layered X65, Mn-doped Fe_3O_4-layered X65 and Zn-doped Fe_3O_4-layered X65 coupons.

Time (h)	Coupons	OCP ($V_{Ag/AgCl}$)	i_{corr} (mA/cm^2)	β_a (mV/decade)	β_c (mV/decade)
4	X65	−0.687	0.136	53.7	246
	Fe_3O_4	−0.670	0.071	58.6	229
	Mg-doped Fe_3O_4	−0.679	0.138	52.0	139
	Mn-doped Fe_3O_4	−0.692	0.113	56.1	227
	Zn-doped Fe_3O_4	−0.642	0.097	61.3	218
24	X65	−0.664	0.170	57.3	264
	Fe_3O_4	−0.673	0.311	57.8	304
	Mg-doped Fe_3O_4	−0.679	0.216	51.5	222
	Mn-doped Fe_3O_4	−0.673	0.253	58.1	244
	Zn-doped Fe_3O_4	−0.678	0.186	68.5	327

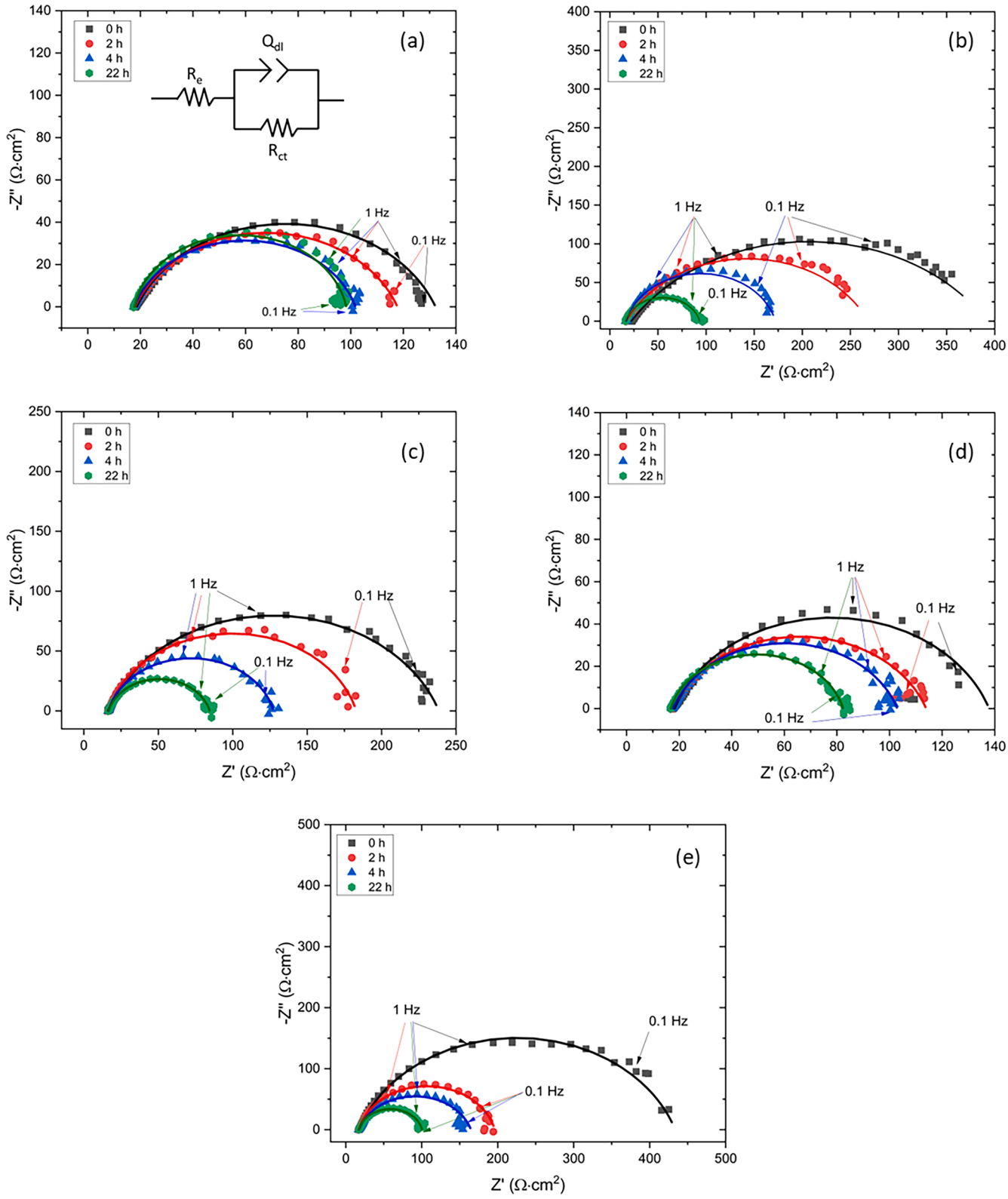

Fig. 8. Nyquist plots from EIS measurements performed in a 50 °C, pH 5, 1 wt% NaCl solution on (a) bare X65 carbon steel, (b) Fe_3O_4-layered X65, (c) Mg-doped Fe_3O_4-layered X65, (d) Mn-doped Fe_3O_4-layered X65 and (e) Zn-doped Fe_3O_4-layered X65 coupons. Solid lines represent the fitted equivalent circuit for each data set. The equivalent electrical circuit shown in (a) is representative of both layered and bare steel coupons. Note: different axis scales are used for each plot.

$$C_{layer} = \frac{\varepsilon_o \varepsilon A}{d} \quad (7)$$

Where ε_o is the vacuum permittivity (8.85×10^{-12} F/m); ε is the relative permittivity of Fe_3O_4, assumed to be 80.5 for Fe_3O_4 (Imran et al., 2018); A is the surface area of the carbon steel coupon (m^2); and d is the thickness of the layer (m) (as determined in Fig. 4).

Therefore, it is suggested that the Fe_3O_4 layers themselves do not contribute significantly to the measured capacitance and the measured capacitance is likely a combination of the double layer capacitance at

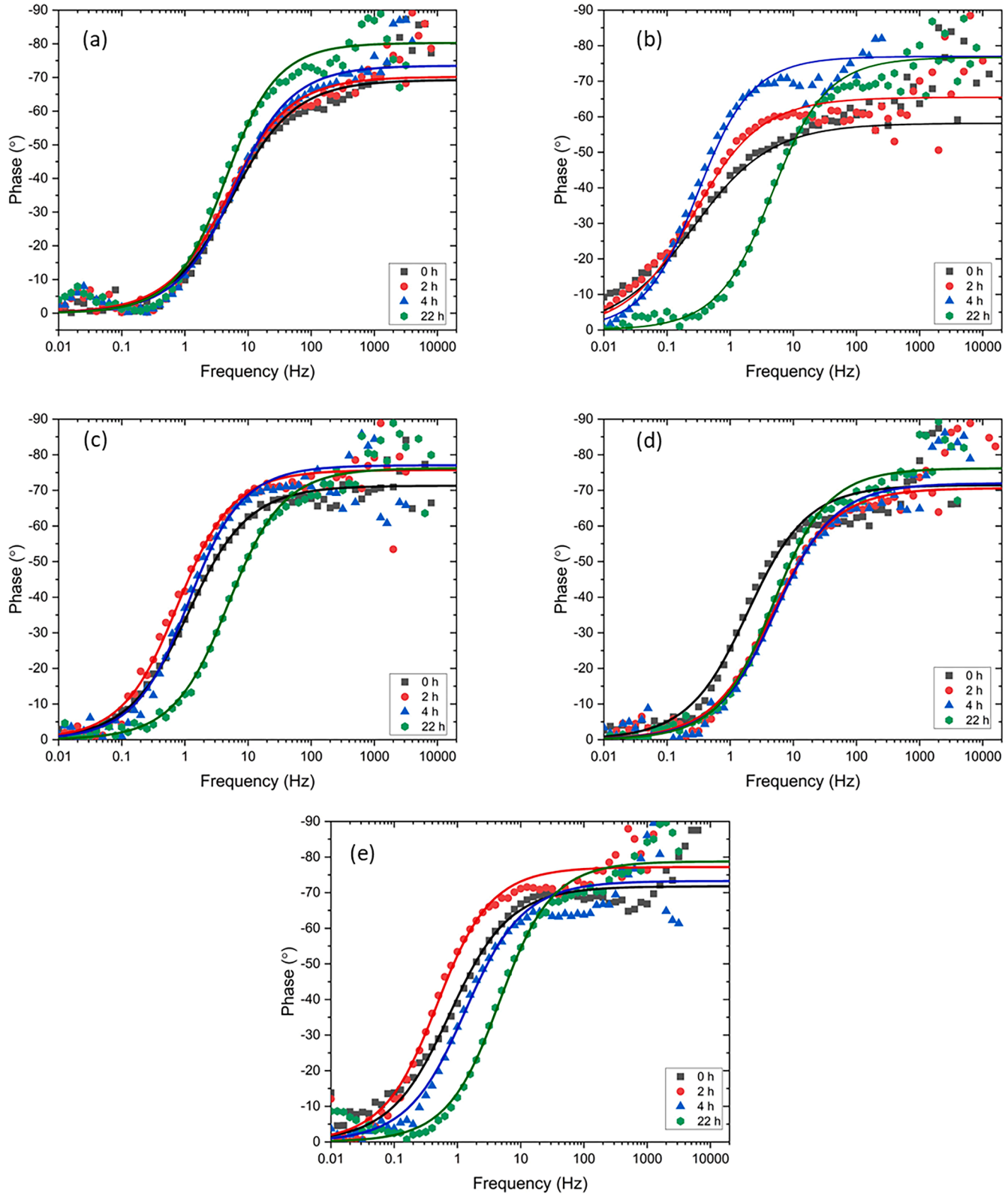

Fig. 9. Phase angle plots from EIS measurements, corrected for solution resistance, performed in a 50 °C, pH 5, 1 wt% NaCl solution on (a) bare X65 carbon steel, (b) Fe_3O_4-layered X65, (c) Mg-doped Fe_3O_4-layered X65, (d) Mn-doped Fe_3O_4-layered X65 and (e) Zn-doped Fe_3O_4-layered X65 coupons.

the surface of regions of Fe_3O_4 and carbon steel.

Alternatively, corrosion product layers on carbon steel, such as thick and well-developed $FeCO_3$ layers in aqueous CO_2 environments, can show a Warburg diffusion impedance in the low frequency domain. This impedance is attributed to the corrosion product layer acting as a diffusion barrier, limiting the transport of species to/from the electrode surface (de Motte et al., 2020; Jacklin et al., 2023). This feature was not observed in Fig. 8, indicating corrosion protection provided by the layers was likely as a result of surface coverage alone, rather than acting as a diffusion barrier. In some experiments, due to the relatively

dynamic nature of the material corrosion behaviour compared to the long acquisition time in the low frequency measurements, some deviation was observed. The emergence of a second capacitance loop at the end of the experiments in some conditions (notably for Zn-doped Fe_3O_4 layers after 22 h) is attributed to adsorbed species on the surface (Keddam et al., 1981). Whilst the adsorption of intermediate species involved in the anodic dissolution of iron is typically observed as an inductive loop, this loop can also be seen as a capacitive loop, often at higher surface pH values in the presence of surface layers form (Keddam et al., 1981). As few data points demonstrated this behaviour, it was omitted from equivalent electrical circuit fitting.

The R_e-corrected phase angle data in Fig. 9 can justify the use of a constant phase element in the proposed equivalent circuit models to fit the X65 steel and layered coupon impedance data. Some dispersion of the data points is observed in this region, due to minor inaccuracies in the determination of R_e. Some data points were not shown where meaningless values were observed after the adjustment. As observed in the high frequency region in Fig. 9, two factors must be considered: 1) the data tend to a value <90° at high and 2) a constant phase angle is generally observed in the 10–100 Hz range (between 70° and 80°). It suggests that a constant phase element is necessary, with the value of φ_{adj} being proportional to the constant phase element α parameter (when α=1, φ_{adj}=90°) (Zhang et al., 2020), most likely as a result of time constant distributions of the double layer capacitance from surface heterogeneities of the rough/roughening X65 steel surface and compositional, crystallographic and/or roughness differences in the layered surfaces.

To investigate the properties identified on the impedance plots in more detail, equivalent electrical circuit fitting was performed on the EIS data. Based on the Nyquist data shapes and the R_e-corrected phase angle plots, it was determined that the interfacial behaviour of the X65 steel and the oxide-layered surfaces could be mathematically represented in a satisfactory manner using a Randles circuit. This equivalent electrical circuit comprises a resistor representing the electrolyte resistance R_e in series with a resistor representing the charge transfer resistance R_{ct} in parallel with a constant phase element, representative of the capacitive behaviour of the electrical double layer (Q_{dl}). Prior to fitting the equivalent electrical circuits, Kramers-Kronig analysis was performed on the data sets and equivalent circuits were only fitted to suitable data. Data points (up to about 5 per experiment) from the highest and lowest frequency ranges were removed from fitting analysis and not shown in the plots in Fig. 8. The fitting is represented by the solid lines on the Nyquist plots in Fig. 8 with fitting data for the all exposure times presented in Table 2 corresponding to the Nyquist plots in Fig. 8 (additional fitting data for each measurement during the 24 h experiment is shown in the Supplementary Material). The effective double layer capacitance (C_{dl}) is determined using the equation developed by Brug et al. (1984), Eq. (8):

$$C_{dl} = \left[Q_{dl} \left(\frac{1}{R_e} + \frac{1}{R_{ct}} \right)^{\alpha - 1} \right]^{\left(\frac{1}{\alpha}\right)} \quad (8)$$

The C_{dl} for bare steel is initially about 130 μF/cm^2, which is consistent with a double layer capacitance of carbon steel in the absence of porous surface layers when immersed in an aqueous solution (Farelas et al., 2010). The increase in C_{dl} observed on bare carbon steel is attributed to the revealing of a porous Fe_3C network, which supports cathodic reactions and significantly increases the electrochemically active surface area (Owen et al., 2022a; 2022b; Farelas et al., 2010). This increase in C_{dl} is not observed on conditions in similar aqueous CO_2-saturated environments when pure iron coupons are utilised and therefore no iron carbide is revealed (Al Kindi et al., 2021). The gradual revealing of the Fe_3C network contributes to the measured decrease in R_{ct} over the experiment for bare carbon steel.

The decrease in R_{ct} over the experiment for the layered coupons confirms the reduced corrosion protection as dissolution of the layers progressed. The release of Fe^{2+} into the pores of the Fe_3O_4 layers as the experiment progressed could have also potentially increased local acidity within the layer, exacerbating dissolution (Park and Macdonald, 1983). A higher value of R_e can be representative of the presence of a thick Fe_3O_4 layer (Park and Macdonald, 1983). Fe_3O_4 dissolution has been shown to previously cause a reduction in R_e as dissolution progressed (Das and Sudersanan, 2003). Although not consistent across all layers, a general decrease in R_e for Fe_3O_4 layers was observed as the layers dissolved.

Table 2
Fitting parameters obtained using a simplified Randles circuit for the data obtained and calculated, where C_{dl} has been calculated using Eq. (8). Full data over the 24 h period (including error) is provided in Supplementary Material. All data was fitted with a $\chi^2 < 10^{-3}$.

Coupon	Time (h)	R_e (Ω cm^2)	R_{ct} (Ω cm^2)	Q_{dl} (μF/cm^2)$^\alpha$	α	C_{dl} (μF/cm^2)
X65	0	18.6	114	564	0.77	138
	2	18.0	100	689	0.78	191
	4	17.7	84	612	0.82	213
	22	17.7	81	631	0.89	358
Fe_3O_4	0	22.2	370	1,943	0.65	337
	2	17.0	251	2,733	0.73	845
	4	17.0	155	3,687	0.86	2,266
	22	16.3	77	739	0.85	333
Mg-doped Fe_3O_4	0	16.2	222	947	0.79	311
	2	16.5	167	1,591	0.84	786
	4	16.6	111	1,677	0.86	897
	22	16.6	68	813	0.85	359
Mn-doped Fe_3O_4	0	18.2	120	1,169	0.79	416
	2	17.7	96	738	0.78	215
	4	17.7	85	718	0.80	230
	22	16.8	65	855	0.85	381
Zn-doped Fe_3O_4	0	17.3	416	696	0.80	224
	2	17.0	179	2,182	0.86	1,244
	4	17.2	148	1,213	0.81	489
	22	17.3	83	631	0.88	323

For the oxide-layered coupons, C_{dl} was generally greater compared against the bare steel coupons at initial exposure times. The C_{dl} for layered coupons, determined using Eq. (8), is compared over the duration of the 24 h experiment for each layer in Fig. 10. The OCP measured over the duration of the experiment is also included. The average C_{dl} and OCP are reported from two measurements with error bars representing the maximum and minimum values. A rapid increase in C_{dl} was observed after immersing the layered coupons in the CO_2-saturated solution, except for Mn-doped Fe_3O_4. From a physico-chemical standpoint, this increase can be explained by the dissolution of the layers, increasing the porosity and therefore the effective electrochemically active surface area. This increase was most significant for the pure Fe_3O_4 layer, likely explained by the marginally superior dissolution resistance of these layers compared to the doped layers. Nonetheless, far greater variation in C_{dl} was observed for these pure Fe_3O_4 layers. The comparison between C_{dl} and OCP also show a strong correlation when identifying the point at which the immersed coupons start to behave in a similar manner to bare carbon steel, where final C_{dl} measurements were shown to be equivalent to bare carbon steel in Table 2. For Fe_3O_4 layers, Fig. 10 shows that the layer influenced the electrochemical behaviour during approximately 12 h before a behaviour like bare carbon steel was observed. For Mg-doped Fe_3O_4 layers this duration was reduced to approximately 8 h and 6 h for Zn-doped Fe_3O_4 layers, whilst Mn-doped Fe_3O_4 layers showed difference in behaviour in the first measurement only.

3.4. Study of localised corrosion

Uniform corrosion protection is advantageous when a surface layer forms on carbon steel. However, in the case of Fe_3O_4, the consequences

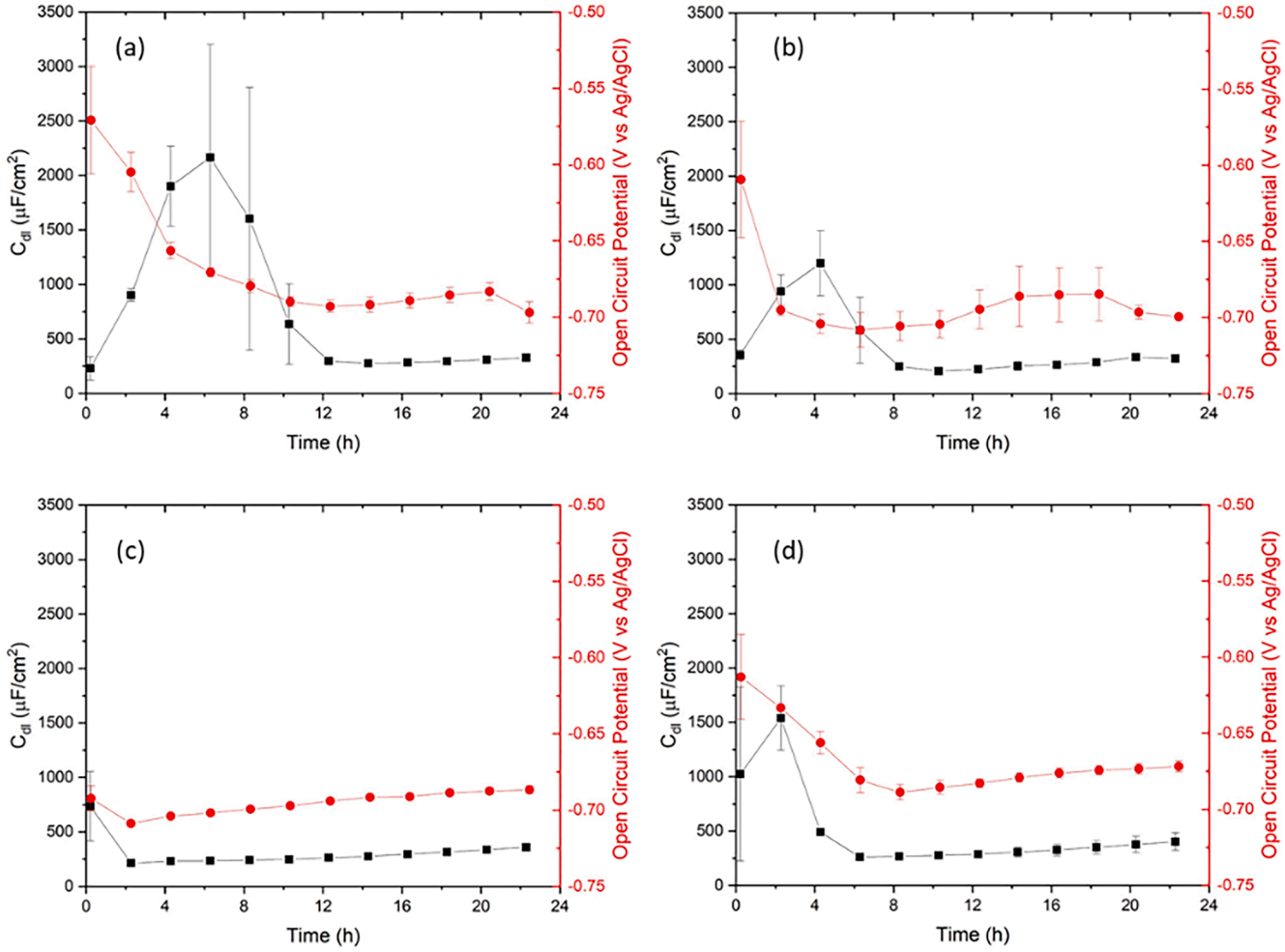

Fig. 10. Double layer capacitance, obtained from EIS measurements, compared with OCP in a 50 °C, pH 5, 1 wt% NaCl solution for (a) Fe_3O_4-layered X65, (b) Mg-doped Fe_3O_4-layered X65, (c) Mn-doped Fe_3O_4-layered X65 and (d) Zn-doped Fe_3O_4-layered X65 coupons.

of localised corrosion, are of great significance. Therefore, localised corrosion analysis was performed at the end of the 24 h experiment to identify any pit-like features that might have developed through any galvanic interaction between the oxide layer and the bare steel. After the experiments, any surface layers were removed in a HCl solution containing HMTA prior to utilising white light interferometry to measure a 3D profile of the surface. Fig. 11 shows 2D surface height maps of 1 mm×1 mm regions on the different coupons studied. The X65 carbon steel covered with Fe_3O_4, Mg-doped Fe_3O_4 and Zn-doped Fe_3O_4 were analysed for the effects of localised corrosion. The Mn-doped Fe_3O_4 layered coupons were excluded from localised corrosion analysis as a result of its lack of uniform corrosion protection, any localised corrosion could not be attributed to the surface layer.

Localised corrosion features (shown by blue deeper regions on the surface maps) were observed on the surface of the steel in the presence of Fe_3O_4 and Zn-doped Fe_3O_4 layers. Fewer localised corrosion features were observed on the surface maps when Mg-doped Fe_3O_4 layers were electrodeposited on the steel surface. To quantify penetration depth, analysis of the top ten deepest pit-like features from three different 1 mm×1 mm regions on the surface is shown in Fig. 11(d). The average penetration depth for carbon steel layered with Fe_3O_4 was 12.1 μm, with a few deeper pit-like features exceeding depths of 15 μm and a maximum penetration depth of ~22 μm. Five pit-like features with a depth more than 10 μm were detected. For comparison to other surface layers commonly found in CO_2 environments, pit-like features observed under $FeCO_3$ on X65 carbon steel at pH 6.8 and 80 °C, after 22 h exposure had an average penetration depth of 5.6 μm with no features exceeding 10 μm in depth (Lazareva et al., 2021), demonstrating the significance of Fe_3O_4 layers on localised corrosion.

Zn-doped Fe_3O_4 layers caused enhanced localised corrosion of the underlying carbon steel. The average penetration depth was 15.7 μm, with a maximum penetration depth of about 20 μm. A total of 21 pit-like features with depths exceeding 10 μm were detected. A previous study by the authors showed that galvanic current between Zn-doped Fe_3O_4 layered X65 and bare X65 carbon steel was greater than pure Fe_3O_4 (Owen et al., 2023). This likely contributed to the enhanced localised corrosion observed in Fig. 11(c). The addition of Mg into the Fe_3O_4 crystal structure appears to have reduced average penetration depth considerably to 9.30 μm and reduced the deepest pit-like features, with a maximum penetration depth of about 11 μm. Only one pit-like feature with a depth more than 10 μm was detected. These results show that the addition of Mg into the Fe_3O_4 crystal structure helped to significantly reduce localised corrosion in the conditions evaluated in this study. Mg-doped Fe_3O_4 layered carbon steel showed similar increases in galvanic current as Zn-doped Fe_3O_4 layered carbon steel when coupled to bare steel, in the same previous study (Owen et al., 2023). However, this did not translate into enhanced localised corrosion. This may be explained by the change in surface coverage over time, with Mg-doped Fe_3O_4 layers appearing to be more persistent than Zn-doped Fe_3O_4 layers in Fig. 10. Mg-doped Fe_3O_4 layers also showed a much quicker decrease in OCP compared to other layers, as shown in Fig. 6, suggesting that significant galvanic corrosion would not have occurred and uniform

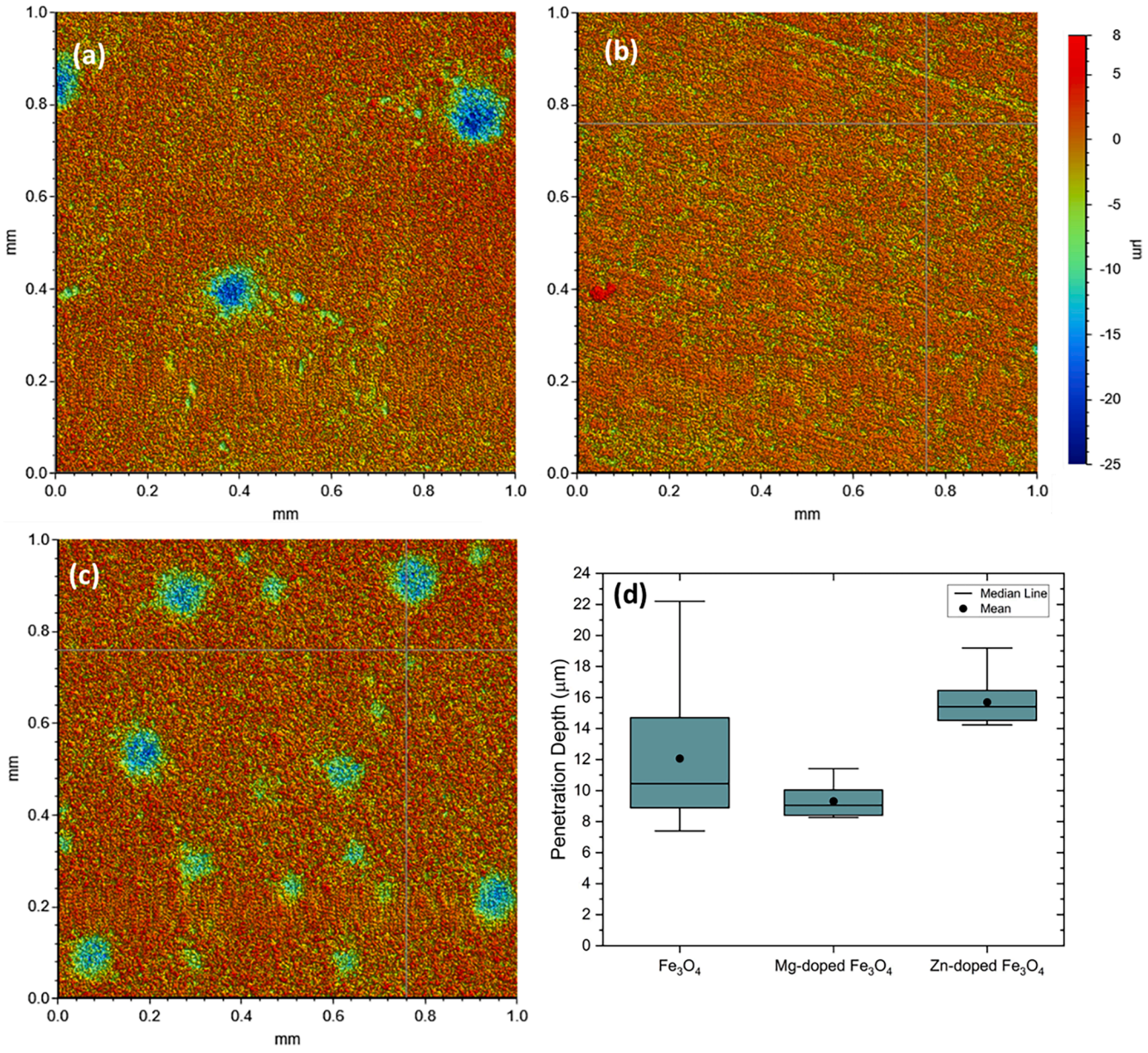

Fig. 11. 3D surface profiles obtained using white light interferometry after 24 h expose to a 50 °C, pH 5, 1 wt% NaCl solution for (a) Fe_3O_4-layered X65, (b) Mg-doped Fe_3O_4-layered X65 and (c) Zn-doped Fe_3O_4-layered X65 coupons. Analysis of the penetration depth for the pit-like features under each surface layer is shown in (d).

corrosion of carbon steel would have proceeded. The persistency of Mg-doped Fe_3O_4 layers, however, was marginally lower than doped Fe_3O_4 layers, as the active surface area and C_{dl} was somewhat lower Fig. 10 and Table 2. Therefore, it is possible that another physical characteristic of the layer, rather than its conductivity, such as its porosity or adherence to the surface may have influenced corrosion protection in this case.

3.5. *Summary of the effect on corrosion behaviour of doping Fe_3O_4*

The results of this study have demonstrated that metal ions can be incorporated into the Fe_3O_4 crystal structure to drive a fundamental change on the corrosion behaviour of carbon steel surfaces covered by such layers. The integration of different metal ions within Fe_3O_4 structures has a significant effect on the morphology of the layers when electrodeposited on carbon steel and has an influence on both uniform and localised corrosion. These results indicated strongly that the addition of Mn into the Fe_3O_4 crystal structure provided no advantages to corrosion protection of carbon steel, when compared to pure Fe_3O_4 structures, in the conditions studied. Mn-doped Fe_3O_4 layers were therefore discarded from any further analysis, showing an inability to offer any corrosion protection to the underlying carbon steel. The lack of protection is potentially explained by instability of the layers in the acidic environment, with leaching of Mn reported from Mn-doped Fe_3O_4 nanoparticles to far exceed leaching of Fe at pH < 6 when immersed in HCl environments (O'Hara et al., 2016). Whilst Mn doping proved to be unsuccessful in this study, it is important to note that natural formation in geothermal waters containing more complex ionic compositions (Mundhenk et al., 2013), could lead to the formation of highly unprotective corrosion product layers, emphasising the importance of understanding the influence of chemical composition on Fe_3O_4 layer formation.

Mg-doped Fe_3O_4 layers showed similar dissolution resistance and levels of corrosion protection to pure Fe_3O_4 layers, with no notable improvements observed. However, the importance of reducing the extent of localised corrosion of carbon steel is paramount, with Fe_3O_4 layers often playing a key role in initiating the growth of pit-like features (Hua et al., 2019), shown in Fig. 11 and in previous studies. Mg doping of Fe_3O_4 layers enabled localised corrosion to be significantly reduced, showing promise as a potential candidate for wider study to deeper probe the mechanisms. Zn-doped Fe_3O_4 layers showed some level of protection in the studied environment, but its performance was reduced compared to Mg-doped Fe_3O_4 and pure Fe_3O_4 layers. An increase in the severity of localised corrosion was also observed.

It should be noted that this study only represents one set of highly corrosive conditions but highlights that Fe_3O_4 layers can be modified to influence the uniform and localised corrosion protection offered by the layer. Studies in higher temperature and pressure conditions more favourable to natural Fe_3O_4 formation would enable layer durability and layer growth mechanisms to be evaluated. However, the implementation of electrodeposition has enabled a methodology to be established for robust and practical analysis of different dopants under numerous, and easily tuneable conditions. The influence of concentration of dopant (Ishikawa et al., 1999), combinations of multiple dopants (de Mello et al., 2019) and the integration of other metal ions (Beal et al., 2017) could also be investigated to optimise layers for specific applications.

4. Conclusions

The corrosion protection provided by Fe_3O_4 layers and Fe_3O_4 modified through the addition of metal ions and formed by electrodeposition on carbon steel surfaces, was assessed in a pH 5, CO_2-saturated, 1 wt% NaCl solution at 50 °C using electrochemical techniques (EIS, LPR and potentiodynamic polarisation). The main findings from the study are:

1) Fe_3O_4 layers on carbon steel surfaces can be modified through the addition of metal ions to change their composition and crystal properties using an electrodeposition method in an electrolyte composed of NaOH, $Fe_2(SO_4)_3$ and TEA through the addition of other metal sulphates.
2) In the thermodynamically unfavourable conditions concerning the dissolution resistance of Fe_3O_4 layers (CO_2-saturated conditions at temperatures of 50 °C), LPR and EIS measurements showed both Fe_3O_4 and doped Fe_3O_4 layers did not provide corrosion protection to the carbon steel throughout the 24 h exposure period, with varying oxide dissolution kinetics.
3) Fe_3O_4 and Mg-doped Fe_3O_4 layers showed the best durability under the conditions studied, maintaining a reduced uniform corrosion rate of the underlying carbon steel for longer than Zn-doped Fe_3O_4 layers, whilst Mn-doped Fe_3O_4 layers provided no corrosion protection.
4) EIS results were justified and modelled using a simplified Randles circuit with no distinct capacitive loop for the layer itself observed; however, EIS analysis confirmed that significant increases in overall capacitance were observed as the layers began to degrade, likely due to increases in active surface area from the conductive oxide and metal surface exposure as the layer dissolved.
5) Localised corrosion was observed on the carbon steel surface underneath the Fe_3O_4 layer (average penetration depth of 12.1 μm), due to the ability of the layer to establish a galvanic couple with bare regions of steel. The addition of Zn dopant into the Fe_3O_4 structure resulted in more severe localised corrosion (average penetration depth of 15.7 μm).
6) The addition of Mg into the Fe_3O_4 crystal structure resulted in significant decreases in localised corrosion of the underlying carbon steel, reducing average penetration depth to 9.30 μm, and recording a maximum penetration depth 50% lower than Fe_3O_4.

CRediT authorship contribution statement

Joshua Owen: Writing – review & editing, Writing – original draft, Methodology, Investigation, Funding acquisition, Formal analysis, Conceptualization. **Francois Ropital:** Writing – review & editing, Supervision, Methodology, Formal analysis. **Gaurav R. Joshi:** Writing – review & editing, Supervision, Methodology, Formal analysis. **Jean Kittel:** Writing – review & editing, Supervision, Resources, Methodology, Formal analysis. **Richard Barker:** Writing – review & editing, Supervision, Resources, Project administration, Methodology, Funding acquisition, Formal analysis, Conceptualization.

Declaration of competing interest

The authors declare that they have no known competing financial interests or personal relationships that could have appeared to influence the work reported in this paper.

Data availability

The raw/processed data required to reproduce these findings cannot be shared at this time as the data also forms part of an ongoing study.

Acknowledgements

The authors would like to acknowledge funding from Engineering and Physical Sciences Research Council (grant number: EP/T009160/1) and the Royal Society (grant number: IES\R1\211068). The authors would also like to thank the contribution from John Harrington and Stuart Micklethwaite at University of Leeds Electron Microscopy and Spectroscopy Centre (LEMAS) and Frederique Perbost-Prigent at IFP Energies Nouvelles.

Supplementary materials

Supplementary material associated with this article can be found, in the online version, at doi:10.1016/j.jpse.2024.100199.

References

Al Kindi, M., Joshi, G.R., Cooper, K., Andrews, J., Arellanes-Lozada, P., Leiva-Garcia, R., et al., 2021. Substrate protection with corrosion scales: can we depend on iron carbonate? ACS Appl. Mater. Interf. 13, 58193–58200.
Alam, M.T., Chan, E.W.L., De Marco, R., Huang, Y., Bailey, S., 2016. Electrochemical and surface analysis studies on the carbon dioxide corrosion of X-65 carbon steel. Electroanalysis. 28 (12), 2910–2921.
ASTM International, 2017. Standard Practice For preparing, cleaning, and Evaluation Corrosion Test Specimens.
Barker, R., Burkle, D., Charpentier, T., Thompson, H., Neville, A., 2018. A review of iron carbonate ($FeCO_3$) formation in the oil and gas industry. Corros. Sci. 142, 312–341.
Basilico, E., Marcelin, S., Mingant, R., Kittel, J., Fregonese, M., Ropital, F., 2021. The effect of chemical species on the electrochemical reactions and corrosion product layer of carbon steel in CO_2 aqueous environment: a review. Mater. Corros. 72 (7), 1152–1167.
Beal, K., Lefèvre, G., Berger, G., Delaunay, S., Goujon, C., Bretelle, J.L., 2017. Electrochemical deposition of magnetite, copper, and mixed magnetite–copper films on nickel-based superalloy substrates. J. Appl. Electrochem. 47 (8), 931–939.
Bhat, M.A., Nioradze, N., Kim, J., Amemiya, S., Bard, A.J., 2017. In Situ detection of the adsorbed Fe (II) Intermediate and the mechanism of magnetite electrodeposition by scanning electrochemical microscopy. J. Am. Chem. Soc. 139 (44), 15891–15899.
Boukamp, B.A., 1995. A linear Kronig-Kramers transform test for immittance data validation. J. Electrochem. Soc. 142 (6), 1885.
Brug, G., van den Eeden, A.L., Sluyters-Rehbach, M., Sluyters, J.H., 1984. The analysis of electrode impedances complicated by the presence of a constant phase element. J. Electroanal. Chem. Interfacial. Electrochem. 176 (1–2), 275–295.
Crolet, J., Thevenot, N., Nesic, S., 1998. Role of conductive corrosion products in the protectiveness of corrosion layers. Corrosion 54 (3), 194–203.
Das, C., Sudersanan, M., 2003. Electrochemical studies of magnetite coating on carbon steel in ascorbic and picolinic acid. J. Appl. Electrochem. 33, 333–338.
de Mello, L.B., Varanda, L.C., Sigoli, F.A., Mazali, I.O., 2019. Co-precipitation synthesis of (Zn-Mn)-co-doped magnetite nanoparticles and their application in magnetic hyperthermia. J. Alloys. Compd. 779, 698–705.

de Motte, R., Basilico, E., Mingant, R., Kittel, J., Ropital, F., Combrade, P., et al., 2020. A study by electrochemical impedance spectroscopy and surface analysis of corrosion product layers formed during CO_2 corrosion of low alloy steel. Corros. Sci. 172, 108666.

Farelas, F., Galicia, M., Brown, B., Nesic, S., Castaneda, H., 2010. Evolution of dissolution processes at the interface of carbon steel corroding in a CO_2 environment studied by EIS. Corros. Sci. 52 (2), 509–517.

Gonzalez, A.H., Frankel, G., Vera, J., Durnie, W., Woollam, R., 2021. Galvanic interactions between Fe electrodes in CO_2-saturated solutions with different pH. Corrosion 77 (11), 1203–1217.

Goujon, C., Pauporté, T., Mansour, C., Delaunay, S., Bretelle, J., 2015. Electrochemical deposition of thick iron oxide films on nickel based superalloy substrates. Electrochim. Acta 176, 230–239.

Han, J., Young, D., Colijn, H., Tripathi, A., Nešić, S., 2009. Chemistry and structure of the passive film on mild steel in CO_2 corrosion environments. Ind. Eng. Chem. Res. 48 (13), 6296–6302.

He, Z., Koza, J.A., Mu, G., Miller, A.S., Bohannan, E.W., Switzer, J.A., 2013. Electrodeposition of $Co_xFe_{3-x}O_4$ epitaxial films and superlattices. Chem. Mater. 25 (2), 223–232.

Hua, Y., Shamsa, A., Barker, R., Neville, A., 2018. Protectiveness, morphology and composition of corrosion products formed on carbon steel in the presence of Cl^-, Ca^{2+} and Mg^{2+} in high pressure CO_2 environments. Appl. Surf. Sci. 455, 667–682.

Hua, Y., Xu, S., Wang, Y., Taleb, W., Sun, J., Zhang, L., et al., 2019. The formation of $FeCO_3$ and Fe_3O_4 on carbon steel and their protective capabilities against CO_2 corrosion at elevated temperature and pressure. Corros. Sci. 157, 392–405.

Imran, M., Akbar, A., Riaz, S., Atiq, S., Naseem, S., 2018. Electronic and structural properties of phase-pure magnetite thin films: effect of preferred orientation. J. Electron. Mater. 47, 6613–6624.

Ishikawa, T., Nakazaki, H., Yasukawa, A., Kandori, K., Seto, M., 1999. Influences of Co^{2+}, Cu^{2+} and Cr^{3+} ions on the formation of magnetite. Corros. Sci. 41 (8), 1665–1680.

Itai, R., Shibuya, M., Matsumura, T., Ishi, G., 1971. Electrical resistivity of magnetite anodes. J. Electrochem. Soc. 118 (10), 1709–1711.

Jacklin, R., Neville, A., Owen, J., Woollam, R.C., Burkle, D., Barker, R., 2022. Iron calcium carbonate formation in CO_2 environments–effects of A/V ratio in autoclave experiments. In: AMPP Annual Conference+ Expo, San Antonio, TX, USA. OnePetro.

Jacklin, R., Owen, J., Burkle, D., Woollam, R.C., Barker, R., 2023. Characterizing the evolution of iron carbonate in a demanding CO_2 environment using a combined electrochemical impedance spectroscopy and linear polarization resistance approach. In: AMPP Annual Conference+ Expo, Denver, CO, USA. AMPP.

Jaffré, K., Abe, H., Ter-Ovanessian, B., Mary, N., Normand, B., Watanabe, Y., 2021. Influence of mechanical surface treatments on oxide properties formed on 304L stainless steel in simulated BWR and PWR primary water. J. Nucl. Mater. 556, 153258.

Jeon, S.H., Song, G.D., Hur, D.H., 2015. Electrodeposition of magnetite on carbon steel in Fe (III)-triethanolamine solution and its corrosion behavior. Mater. Transact. 56 (7), 1107–1111.

Karadag, A., Yilmaz, V.T., Thoene, C., 2001. Di-and triethanolamine complexes of Co (II), Ni (II), Cu (II) and Zn (II) with thiocyanate: synthesis, spectral and thermal studies. Crystal structure of dimeric Cu (II) complex with deprotonated diethanolamine,$[Cu_2(\mu\text{-dea})_2(NCS)_2]$. Polyhedron. 20 (7–8), 635–641.

Keddam, M., Mattos, O.R., Takenouti, H., 1981. Reaction model for iron dissolution studied by electrode impedance: II. Determination of the reaction model. J. Electrochem. Soc. 128 (2), 257–266.

Ko, M., Ingham, B., Laycock, N., Williams, D.E., 2015. In situ synchrotron X-ray diffraction study of the effect of microstructure and boundary layer conditions on CO_2 corrosion of pipeline steels. Corros. Sci. 90, 192–201.

Kothari, H.M., Kulp, E.A., Limmer, S.J., Poizot, P., Bohannan, E.W., Switzer, J.A., 2006. Electrochemical deposition and characterization of Fe_3O_4 films produced by the reduction of Fe (III)-triethanolamine. J. Mater. Res. 21 (1), 293–301.

Kulp, E.A., Kothari, H.M., Limmer, S.J., Yang, J., Gudavarthy, R.V., Bohannan, E.W., et al., 2009. Electrodeposition of epitaxial magnetite films and ferrihydrite nanoribbons on single-crystal gold. Chem. Mater. 21 (21), 5022–5031.

Lazareva, A., Owen, J., Vargas, S., Barker, R., Neville, A., 2021. Investigation of the evolution of an iron carbonate layer and its effect on localized corrosion of X65 carbon steel in CO_2 corrosion environments. Corros. Sci. 192, 109849.

Lê, A., Floner, D., Roisnel, T., Cador, O., Chancelier, L., Geneste, F., 2019. Highly soluble Fe (III)-triethanolamine complex relevant for redox flow batteries. Electrochim. Acta 301, 472–477.

Matamoros-Veloza, A., Barker, R., Vargas, S., Neville, A., 2020. Iron calcium carbonate instability: structural modification of siderite corrosion films. ACS Appl. Mater. Interf. 12 (43), 49237–49244.

Mercier-Bion, F., Li, J., Lotz, H., Tortech, L., Neff, D., Dillmann, P., 2018. Electrical properties of iron corrosion layers formed in anoxic environments at the nanometer scale. Corros. Sci. 137, 98–110.

Mundhenk, N., Carrero, S., Knauss, K., Wonneberger, R., Undisz, A., Wu, Y., 2020. Kinetic and thermodynamic analysis of high-temperature CO_2 corrosion of carbon steel in simulated geothermal NaCl fluids. Corros. Sci. 171, 108597.

Mundhenk, N., Huttenloch, P., Kohl, T., Steger, H., Zorn, R., 2013. Metal corrosion in geothermal brine environments of the upper Rhine graben–laboratory and on-site studies. Geothermics. 46, 14–21.

O'Hara, M.J., Carter, J.C., Warner, C.L., Warner, M.G., Addleman, R.S., 2016. Magnetic iron oxide and manganese-doped iron oxide nanoparticles for the collection of alpha-emitting radionuclides from aqueous solutions. RSC. Adv. 6 (107), 105239–105251.

Orazem, M.E., Tribollet, B., 2008. Electrochemical Impedance Spectroscopy. Wiley, Hoboken, N.J.

Orooji, Y., Haddad Irani-nezhad, M., Hassandoost, R., Khataee, A., Rahim Pouran, S., Joo, S.W., 2020. Cerium doped magnetite nanoparticles for highly sensitive detection of metronidazole via chemiluminescence assay. Spectrochim. Acta Part A Mol. Biomol. Spectrosc. 234, 118272.

Owen, J., Ropital, F., Joshi, G., Kittel, J., Barker, R., 2022a. Galvanic interactions between surface layers and bare carbon steel in aqueous CO_2 environments. In: AMPP Annual Conference + Expo. AMPP, San Antonio, TX, USA.

Owen, J., Ropital, F., Joshi, G.R., Kittel, J., Barker, R., 2022b. Galvanic effects induced by siderite and cementite surface layers on carbon steel in aqueous CO_2 environments. Corros. Sci. 209, 110762.

Owen, J., Ropital, F., Joshi, G.R., Kittel, J., Jacklin, R., Burkle, D., et al., 2023. Modified magnetite surface layers on carbon steel in aqueous CO_2 environments. In: AMPP Annual Conference+ Expo. AMPP, Denver, CO, USA.

Park, J., Macdonald, D., 1983. Impedance studies of the growth of porous magnetite films on carbon steel in high temperature aqueous systems. Corros. Sci. 23 (4), 295–315.

Sanjuan, B., Millot, R., Innocent, C., Dezayes, C., Scheiber, J., Brach, M., 2016. Major geochemical characteristics of geothermal brines from the Upper Rhine Graben granitic basement with constraints on temperature and circulation. Chem. Geol. 428, 27–47.

Sen, B., Dotson, R.L., 1970. Characterization and studies of some triethanolamine complexes of transition and representative metals. J. Inorgan. Nucl. Chem. 32 (8), 2707–2716.

Shaikhah, D., Barker, R., Taleb, W., Lazareva, A., Mohamed-Said, M., Cowe, B., et al., 2022. Engineering of corrosion product-polymer hybrid layers for enhanced CO_2 corrosion protection of carbon steel part one: corrosion study and mechanical property investigation. Polymer. (Guildf) 242, 124614.

Shamsa, A., Barker, R., Hua, Y., Barmatov, E., Hughes, T.L., Neville, A., 2019. The role of Ca^{2+} ions on Ca/Fe carbonate products on X65 carbon steel in CO_2 corrosion environments at 80 and 150 °C. Corros. Sci. 156, 58–70.

Song, G.D., Jeon, S.H., Son, Y.H., Kim, J.G., Hur, D.H., 2018. Galvanic effect of magnetite on the corrosion behavior of carbon steel in deaerated alkaline solutions under flowing conditions. Corros. Sci. 131, 71–80.

Suresh, S., Rangarajan, S., Bera, S., Krishnan, R., Kalavathi, S., Velmurugan, S., 2016. Electrochemical characterization of nano zinc ferrite coating on carbon steel by pulsed laser deposition. Thin. Solid. Films. 612, 250–258.

Sweeton, F., Baes Jr, C., 1970. The solubility of magnetite and hydrolysis of ferrous ion in aqueous solutions at elevated temperatures. J. Chem. Thermodyn. 2 (4), 479–500.

Switzer, J.A., Gudavarthy, R.V., Kulp, E.A., Mu, G., He, Z., Wessel, A.J., 2010. Resistance switching in electrodeposited magnetite superlattices. J. Am. Chem. Soc. 132 (4), 1258–1260.

Tanupabrungsun, T., Brown, B., Nesic, S., 2013. Effect of pH on CO_2 corrosion of mild steel at elevated temperatures. In: CORROSION 2013. NACE International, Orlando, FL, USA.

Tanupabrungsun, T., Young, D., Brown, B., Nešic, S., 2012. Construction and verification of pourbaix diagrams for CO_2 corrosion of mild steel valid up to 250 °C. In: CORROSION 2012. NACE International, Salt Lake City, UT, USA.

Thorhallsson, A.I., Stefansson, A., Kovalov, D., Karlsdottir, S.N., 2020. Corrosion testing of materials in simulated superheated geothermal environment. Corros. Sci. 168, 108584.

Verwey, E., Heilmann, E., 1947. Physical properties and cation arrangement of oxides with spinel structures I. Cation arrangement in spinels. J. Chem. Phys. 15 (4), 174–180.

Watson, W., Orazem, M.E., 2020. EIS: measurement model program.

Xu, Y., Schoonen, M.A., 2000. The absolute energy positions of conduction and valence bands of selected semiconducting minerals. Am. Mineral. 85 (3–4), 543–556.

Zhang, Z., Ter-Ovanessian, B., Marcelin, S., Normand, B., 2020. Investigation of the passive behavior of a Ni–Cr binary alloy using successive electrochemical impedance measurements. Electrochim. Acta 353, 136531.